

Low T_c Hafnium Kinetic Inductance Device with High Internal Quality Factor

Xinran Li,^{1, a)} Aritoki Suzuki,¹ and Maurice Garcia-Sciveres¹
Lawrence Berkeley National Laboratory, Berkeley, CA, USA

(Dated: 28 February 2025)

Kinetic inductance devices (KIDs) are superconducting resonators with high kinetic inductance sensitive to external energy perturbations. KIDs made with superconductors having T_c far below one Kelvin are of particular interest for sensing minuscule signals, such as light dark matter detection and millimeter wave telescopes for astronomy and cosmology. In this work, we report the promising performance of KIDs fabricated with Hafnium from heated sputter depositions. The KIDs have T_c lower than (249 ± 2) mK, the internal quality factor (Q_i) of the resonators exceeds 10^5 and the temperature dependence of the resonances can be described by the generalized Mattis-Bardeen model with a disorder parameter $\Gamma = 4 \times 10^{-3} \Delta_0$. Post-fabrication annealing at temperatures above the deposition temperature can further reduce the T_c and Γ without reducing Q_i , leading to improvements in energy resolution.

Kinetic inductance devices (KIDs) are superconducting resonators microfabricated from thin films with high kinetic inductance. KIDs have broad applications in astronomy^{1,2}, cosmology³, and particle physics⁴⁻⁶. They can be designed as quantum sensors to detect single photons^{7,8} or multiplexing readout for detector arrays^{9,10}.

Recently, using KIDs as dark matter direct detectors has been revitalized^{5,6} as the field shifts the focus to light dark matter (DM) candidates with mass below $1 \text{ GeV}/c^2$, which requires low energy threshold technologies beyond conventional ionizing or scintillating detectors¹¹⁻¹³. KIDs are sensitive to $O(1) \sim O(100)$ meV athermal phonons produced by energy deposited in the crystal substrates they are built on, which makes them sensitive to sub-GeV DM interactions¹⁴. Currently, the most sensitive athermal phonon detectors are built with transition edge sensors (TESs)¹⁵, and they have been implemented in multiple light DM experiments¹⁶⁻¹⁸. Since TESs require superconducting quantum interference device (SQUID) amplifiers as the low-noise, low-impedance readout, scaling in detector mass and reading out large TES arrays is challenging. In comparison, KIDs operate in radio frequency (RF), which is naturally multiplexible. They have the potential to achieve sub-eV energy thresholds and the scalability to thousands of channels for the next-generation kilogram detectors.

Among the various materials that have been explored¹⁹, materials with low critical temperatures (T_c) are preferred for sensing, as more quasiparticles will be produced per unit of energy. A high internal quality factor (Q_i) further magnifies the small change in resonance frequency. Previously, Aluminum (Al) KIDs have been widely studied with $T_c = 1.2 \text{ K}$ and consistently achieved high Q_i around 10^6 . Recent works⁸ demonstrated the possibility of detecting single THz photons with Al KIDs. The responsivity is significantly boosted by reducing the inductor volume to nm^3 scale. However, this approach requires attaching an antenna to the inductor to increase the collection area and focusing photons onto the antenna, which does not trivially apply to an athermal phonon detector.

Similarly to an antenna for electromagnetic waves, an Al phonon absorber coupling to the KID with a quasiparticle trap²⁰ can collect phonons, but it requires even lower T_c KIDs. Quasiparticle trapping significantly improves phonon collection efficiency while maintaining a small inductor volume and high responsivity. This technique has been successfully demonstrated in TESs^{21,22}, with Al as the phonon absorber and Tungsten as TESs. It also has been demonstrated in X-ray KID detectors, with Tantalum (Ta) as the photon absorber and Al as KIDs²³. Al is perfect for the high- T_c phonon absorber in a quasiparticle trap, as it has a long quasiparticle lifetime²⁴ and a matched acoustic impedance to common substrates such as Si. We are therefore searching for KID materials with T_c much less²⁴ than 1.2 K, high Q_i , high kinetic inductance, and fabrication compatibility for DM KID detector development.

Low T_c materials such as β -Ta, Osmium, Titanium, Hafnium (Hf), and Iridium have been explored¹⁹, among which we consider Hf the most promising candidate due to its suitable T_c , high kinetic inductance, and high Q_i . Previous works on Hf KIDs^{2,25} have demonstrated large pixel arrays that can resolve 1 eV IR photons.

We have obtained promising results with KIDs fabricated from Hf using a novel heated sputter deposition process on silicon substrates²⁶. A T_c of 250 mK has been achieved with a surface inductance of $4.8 \text{ pH}/\square$. The Q_i of the resonators is higher than 10^5 , sufficient for use as phonon sensors. Notably, the T_c can be tuned post-fabrication with an annealing process, allowing precise tuning of device performance. Adding the quasiparticle trapping technique to such Hf KIDs would lead to sub-eV threshold phonon-sensing detectors.

The Hf films in this study are 250 nm thick, deposited with plasma sputtering on Si substrates heated to 200°C . We chose the thickness as it is an established fabrication process from previous work on Hf-TESs development for cosmic microwave background detectors²⁶; we will reduce the thickness in the future to achieve higher surface kinetic inductance. The T_c of the film lowers linearly as the substrate temperature increases during deposition. Above 550°C , the film T_c approaches bulk Hf T_c of 128 mK ²⁷. We chose a 200°C deposition temperature for T_c at 250 mK, which allowed us to reliably operate KIDs fabricated from the films in a dilution refrigerator (DR). A chlorine-based plasma etching is used to

^{a)}Email: xinranli@lbl.gov

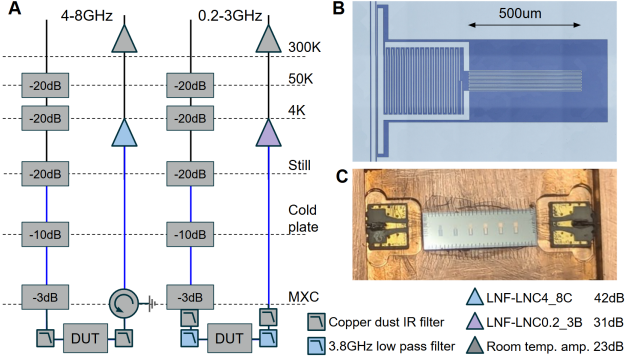


FIG. 1. **A)** Cold electronics of the two frequency bands. DUT refers to the KID housed in the copper box. **B)** Example microscope picture the KID. Light blue is Hf and dark blue is exposed silicon. **C)** Picture of the KID chip mounted in the copper box with rubber cement.

pattern the film into KIDs.

At such low T_c , the pair-breaking energy is $2 \times 1.76k_B T_c = 76 \mu\text{eV}$, corresponding to 18.4 GHz photons. For the interest of sensor design, the KID frequency should be as low as possible to minimize parasitic quasiparticle excitations by the readout power²⁸. Here, we designed 12 lumped element KIDs with resonances from 1.8 GHz up to 6 GHz to test the quasiparticle dynamics under different readout frequencies. They share the same interdigitated capacitor design and vary in the inductor dimensions, as shown in Fig. 1.B. They are distributed across two chips, the six resonators in the lower frequency band from 1.8 GHz to 3 GHz have 8 mm long meandering inductors with width ranging from $3 \mu\text{m}$ to $12 \mu\text{m}$. The six resonators in the high-frequency band have 2 mm long inductors with the same width that matches each of the low-frequency resonators. Fig. 1.B shows the 1.8 GHz KID design as an example.

The KIDs were cooled by a DR and readout with two high electron mobility transistor (HEMT) amplifiers. Extra attention was exercised to reduce parasitic RF power loading on the low- T_c KIDs. Details of the RF circuit is shown in Fig. 1.A, and further described in the supplementary material. The chips were mounted in an IR light-tight copper box with a $20 \times 20 \times 5 \text{mm}$ cavity using rubber cement. The copper box lid has a step that mates tightly to the edge of the cavity. Each end of the feedline was wire bonded to a small PCB that was soldered to the SMA connector. Wire bonds were added from the ground plane to the copper box to ensure good grounding, as shown in Fig. 1.C.

A vector network analyzer was used to pinpoint the resonant frequency of each KID and measure the I-Q response of signal transmission, S_{21} . Measurements were performed on each KID at temperatures from 10 mK to 60 mK, and readout powers changing in steps of 5 dB. The resonances were scanned twice with increasing and decreasing frequencies to capture non-linear kinetic inductance behavior at high readout powers.

An example scan of the lowest frequency KID is shown in Fig. 2. The top panels show the dependence on temperature

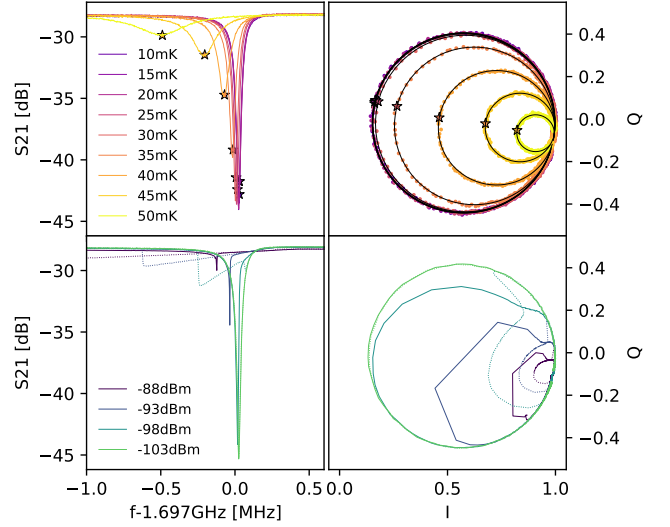


FIG. 2. Example S_{21} (left panels) and I-Q (right panels) scan for the KID in Fig. 1B. Top panels show the scan with -113 dBm readout power at various bath temperatures. Black curves are the best fit of Eq. 8 and the star marks the point at f_r . The bottom panels show the scan with various readout power at 20 mK. Solid lines are ascending frequency scans, dashed lines are descending frequency scans. Differences in the two scanning directions due to quasiparticle heating are observed with $P_{\text{feed}} > 103 \text{ dBm}$.

while the readout power is relatively low, -113 dBm on the feedline. This power, P_{feed} , is estimated with cable loss corrections. We attribute the $10 \sim 15 \text{ dB}$ additional attenuation measured on the VNA at off-resonance frequencies to cable loss and assume half of it occurs before the chip. Unless specified otherwise, all absolute power values mentioned hereafter refer to the power on the feedline, and they are associated with $\pm 2 \text{ dB}$ uncertainty. After each scan, we fit the resonant circle in the I-Q plane to extract Q_i and f_r ; see supplement material for the fitting function.

The bottom panels of Fig. 2 show the scans of the same KID with higher powers. Significant nonlinearity is observed for powers above -103 dBm , which results in hysteresis when scanning frequencies in different directions. Two known effects can induce nonlinearity: one is a large current generating magnetic field that changes the gap energy²⁹, and the other is quasiparticle heating by the readout power³⁰. A rough estimation suggests that the second effect occurs first in the low- T_c Hf KID; see supplementary material for details.

We restrict the discussion below to the linear behavior of Hf KIDs. We find that the readout power most easily saturates the KID with the lowest resonant frequency, and the highest power without hysteresis is around -100 dBm . The following results are restricted to readout powers below -110 dBm , so that the quasiparticles are not significantly disturbed.

The most essential parameters are the kinetic inductance of the Hf film, L_k , and the internal quality factor, Q_i . We estimated L_k by comparing the measured resonant frequencies at 10 mK to simulation results. We used SONNET³¹ to simulate the RF field with L_k parametrized as the surface inductance

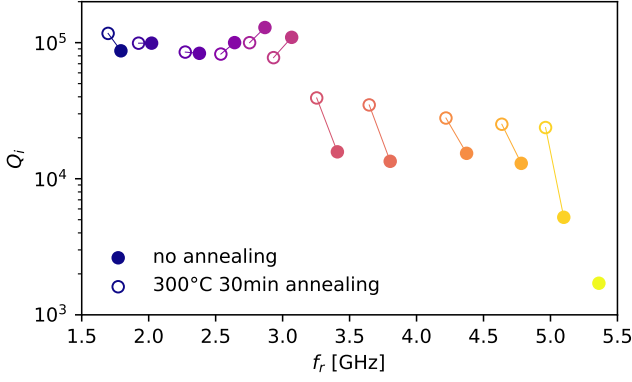


FIG. 3. Q_i at 10 mK and -118 dBm readout power of KIDs with (open circle) and without (closed circle) annealing. KIDs of the same design are connected by thin lines to guide the eye. The highest frequency resonator on the annealed chip had a defect, and no resonance was observed.

of a perfect conductor³². The best agreement across all KIDs was achieved with $L_k = (4.8 \pm 0.1)$ pH/ \square . For comparison, we can estimate L_k from the normal resistance, assuming the thin film limit³³.

$$L_k = \mu_0 \lambda_{\text{thin}} \approx \mu_0 \frac{105 \text{ nm}^2}{t} \frac{R_n t}{1 \mu\Omega \text{ cm}} \frac{1 \text{ K}}{T_c} \quad (1)$$

where $\mu_0 = 4\pi \times 10^{-7}$ H/m is the vacuum permeability, t is the film thickness and here $t = 250$ nm, and R_n is the normal sheet resistance. We measured $T_c = (249 \pm 2)$ mK and $R_n = (0.86 \pm 0.03)$ Ω/\square at 1 K with a AC resistance bridge. The resulting L_k is (4.8 ± 0.1) pH/ \square , agrees well with the measurement from resonances.

As mentioned in the introduction, the T_c of Hf can be tuned post-fabrication with annealing at temperatures above the original deposition temperature. We annealed one set of chips at 300 °C in an Argon environment for 30 minutes. The T_c of the annealed chip dropped to (233 ± 2) mK while the normal resistance decreased to (0.83 ± 0.03) Ω/\square . Eq. 1 suggests L_k increases to (4.9 ± 0.1) pH/ \square and the measured value is (5.3 ± 0.1) pH/ \square .

The Q_i values at 10 mK are summarized in Fig. 3. KIDs in the low-frequency band have Q_i close to or exceeding 10^5 , which will provide excellent energy resolution as phonon sensors. No significant reduction of Q_i was observed with annealing. Rather, annealed KIDs in the high-frequency band have higher Q_i , which is most likely caused by systematics in the measurement environment, since the no-annealing data was taken five days after the DR reached 1 K, while the annealed data was taken 20 days after. The circulator, which only presented in the high-frequency band, might not have reached thermal equilibrium with the DR in five days, allowing thermal photon emission to back-propagate to the KID and reduce the Q_i .

The dependence of the complex conductivity on frequency and temperature, $\sigma(\omega, T) = \sigma_1(\omega, T) - i\sigma_2(\omega, T)$, defines the responsivity of KIDs. J. Gao et. al. demonstrated

the equivalence of thermally and external energy excited quasiparticles³⁴, as shown by Fig. 1 in the reference³⁴

$$\frac{d\sigma_{1,2}}{dE} = \frac{dn_{\text{qp}}}{dE} \frac{d\sigma_{1,2}}{dn_{\text{qp}}} = \frac{dn_{\text{qp}}}{dE} \frac{\partial \sigma_{1,2}(T)/\partial T}{\partial n_{\text{qp}}(T)/\partial T} \quad (2)$$

where E is the external signal energy deposition in the quasiparticle system, and n_{qp} is the quasiparticle density.

We characterize $\sigma_{1,2}(\omega, T)$ by measuring the temperature dependence of the resonant frequencies and quality factors. To compare results from different KIDs and materials, we follow N. Zobrist, *et al.*², and define the normalized fractional change of frequency, $2\delta f_r/f_{r0}/\alpha\gamma$, and the quality factor, $\delta(1/Q)/\alpha\gamma$, where δ means the variance relative to the zero temperature value, and α is the kinetic inductance fraction, which can be calculated from simulation, and $\gamma = 1$ in the thin film approximation. Since the coupling quality factor Q_c is a constant, $\delta(1/Q) = \delta(1/Q_i)$. The fractional changes directly relate to $\delta\sigma_{1,2}$ as

$$2\delta f_r/f_{r0}/\alpha\gamma = (\sigma_2(T) - \sigma_2(0))/\sigma_2(0) \quad (3)$$

$$\delta(1/Q)/\alpha\gamma = \sigma_1(T)/\sigma_2(T) - \sigma_1(0)/\sigma_2(0) \quad (4)$$

The BCS theory and the Mattis-Bardeen (M-B) model³⁵ give the theoretical form of $\sigma_{1,2}(T)$ and $n_{\text{qp}}(T)$ in ideal superconductors. Here, we follow Nam's generalization to parametrize the state broadening due to disorders by the parameter Γ ^{36,37}. Other physically motivated generalizations lead to formulas with subtle differences; see supplement materials for detailed treatment of the generalized M-B model.

The temperature dependence of the fractional changes is shown in Fig. 4. KIDs without annealing are best fit with $\Gamma = 4 \times 10^{-3}\Delta_0$, and the annealed KIDs suggests a reduced best-fit value of $\Gamma = 1.5 \times 10^{-3}\Delta_0$. The difference in Γ is most visible around $T = 0.15T_c$, where higher disorders (larger Γ) cause the frequency shift to start at lower temperatures before the Q_i starts to degrade. However, this observation does not imply that a more disordered film would exhibit a stronger phase signal response.

The model also qualitatively predicts the frequency dependence. The measurements span a wide frequency range, from $0.2\Delta/h$ to $0.6\Delta/h$, showing clear frequency dependence in $\sigma_{1,2}$. At high temperatures, high-frequency KIDs have less $\delta f_r/f_{r0}$. But at intermediate temperatures, especially for a large Γ , the trend reverses, and high-frequency KIDs have greater $\delta f_r/f_{r0}$.

Previous work² on Hf KIDs used a different generalization, which also fits the data qualitatively. In this work, the best-fit suggests a superconducting gap closer to the BCS value of $1.762k_B T_c$ and a smaller Γ , suggesting less disorder in the film, which is further reduced after annealing. The difference may be attributed to the different film deposition procedures.

The energy response of the KID can be estimated from the transmission, S_{21} . Using Eq. 2 to 4, the perturbation of S_{21} due to small energy can be written as

$$\delta S_{21} = \frac{Q_r^2}{Q_c} \alpha\gamma \left[i \frac{d\sigma_2/dn_{\text{qp}}}{\sigma_2(0)} + \frac{d\sigma_1/dn_{\text{qp}}}{\sigma_2(0)} \right] \frac{dN_{\text{qp}}}{dE} \frac{1}{V} \delta E \quad (5)$$

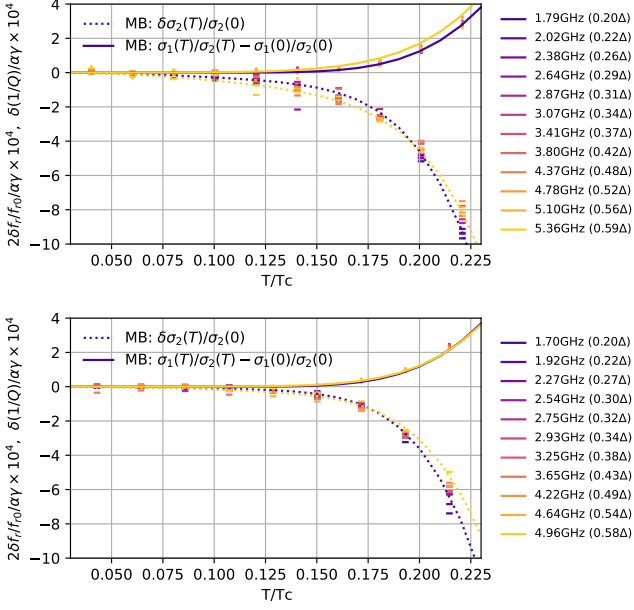


FIG. 4. Normalized fractional change of resonant frequencies and internal quality factors vs temperature. Short bars and dots are the fitting results of f_r and Q_i , respectively, for each KID at different temperatures. A darker color corresponds to KID with a lower resonant frequency. Solid and dashed curves represent the generalized M-B model of the normalized fractional change of Q_i and f_r , respectively. **Top:** Chip with no treatment. Best described with $\Gamma = 4 \times 10^{-3} \Delta_0$. **Bottom:** Chip annealed at 300 °C for 30min in an Argon environment. Best described with $\Gamma = 1.5 \times 10^{-3} \Delta_0$.

The energy collection efficiency η is included in the term $dN_{qp}/dE = \eta/\Delta$, where η includes all the efficiencies for converting the signal energy into a number of excited quasiparticles. V is the sensitive volume of the KID's inductor, and a smaller volume is preferred for a higher response.

The numerical shape of $d\sigma_{1,2}/dn_{qp}/\sigma_2(0)$ can be derived from the model we built and tested in Fig. 4. Results are shown in Fig. 5. Positive curves show the dissipation response, $d\sigma_1/dn_{qp}/\sigma_2(0)$, while negative curves show the phase response, $d\sigma_2/dn_{qp}/\sigma_2(0)$. In addition to the best-fit Γ values, situations with $\Gamma = 0$ and $\Gamma = 10^{-5}$ are shown for reference. The solid and thin dashed curves were calculated with $f_r = 2$ GHz and $f_r = 4$ GHz, respectively. Reducing the resonance frequency improves the signal response. Although $\partial\sigma/\partial T$ increases as Γ increases, the density of states below the gap increases as well, resulting in a higher n_{qp} and higher $\partial n_{qp}/\partial T$ that do not exponentially decay as T approaches zero. In other words, more quasiparticle excitations are needed to fill the sub-gap states to generate the same effective temperature change compared to a $\Gamma = 0$ ideal superconductor. Thus, a small Γ is preferred to achieve a high signal response in a KID. In this work, the annealed chip presents a lower Γ , and it should achieve the highest response around $T = 0.15 \sim 0.2T_c$. The Q_i reduction becomes significant as T approaches $0.2T_c$, and it will suppress δS_{21} as Q_r^2 .

Note that the previous discussion assumes the density of

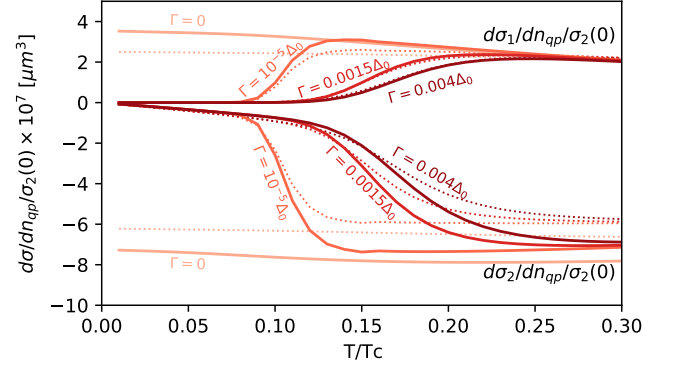


FIG. 5. Signal response prediction from the generalized M-B theory. Positive and negative curves correspond to dissipation signal ($d\sigma_1/dn_{qp}/\sigma_2(0)$) and phase signal ($d\sigma_2/dn_{qp}/\sigma_2(0)$), respectively. Solid and dashed curves are response of KIDs at 2 GHz and 4 GHz, respectively. From light to dark, the disorder parameter Γ increases. The $\Gamma = 0$ curve takes the approximated analytical form from J. Gao³⁴, as the numerical differential calculations diverge. Annealing reduces Γ and increases signal response.

states after broadening has the Lorentzian shape down to zero energy. However, other models with different distributions have been proposed³⁸. The complex conductance measurement with resonators is not sensitive enough to distinguish between the various models. And the actual behavior of $\partial n_{qp}/\partial T$ may differ. Generally speaking, any density of states broadening will increase $\partial n_{qp}/\partial T$ close to zero temperature, reducing the response.

Another implicit assumption is that the quasiparticle distribution is thermal, which might not be a precise description. Various experiments³⁹ have observed quasiparticle lifetimes diverging from the BCS theory as the superconductor being cooled, indicating a significant population of residue quasiparticles. Conventional treatment includes introducing an effective chemical potential³⁴, and assuming they follow a thermal distribution. In addition, the readout microwave can also alter the quasiparticle distribution and break Cooper pairs through multiphoton processes, preventing the predicted noise equivalent power from being achieved²⁸. With all the theoretical uncertainties, the prediction of KID sensitivity remains a challenging task. Further studies with energy calibrations will improve the understanding.

In conclusion, we measured the performance of KIDs fabricated from Hf films deposited on heated silicon substrates. The T_c of a 250 nm film deposited at 200 °C is (249 ± 2) mK. Post-fabrication annealing reduces the T_c to (233 ± 2) mK and raises the sheet kinetic inductance from (4.8 ± 0.1) pH/ \square to (5.3 ± 0.1) pH/ \square . The complex conductivity of Hf was carefully characterized at temperatures from 10 mK to $0.25T_c$ from resonance measurements of KIDs operated at frequencies from $0.17\Delta/h$ to $0.6\Delta/h$. The temperature and frequency dependence can be well described by the generalized M-B theory with the state broadening parameter Γ . Notably, annealing also reduces Γ from $4 \times 10^{-3} \Delta_0$ to $1.5 \times 10^{-3} \Delta_0$, which hints to an improvement in the energy response.

We have demonstrated the potential of Hf fabricated by heated sputter deposition as a promising candidate for phonon sensing KIDs for light DM searches. Specifically, the low T_c allows it to form quasiparticle trapping structures with Al phonon absorbers to improve phonon collection efficiency significantly while maintaining high signal response. Results from this work suggest annealing as a powerful tool to adjust the material properties and potentially improve the sensor performance.

On the other hand, theoretical uncertainties in describing disordered superconductors persist. Further studies, such as quasiparticle lifetime measurement, energy calibration, and noise characterization will reveal more profound insights.

I. SUPPLEMENTARY MATERIAL

RF circuit. The 12 KIDs of the two bands were grouped on two chips and readout by an LNF-LNA0.2-3B and an LNF-LNA4-8F HEMT amplifier separately. Details of the readout circuit are shown in Fig. 1.A. Extra attention was exercised to reduce parasitic RF power loading on the low- T_c KIDs. A total of 73 dB attenuation was added to the input line to minimize thermal photons emitted at higher temperature from reaching the KIDs. Copper dust filters (Quantum Microwave QMC-CRYOIRF-003MF-S) were installed on both sides of the test box to filter photons at 10 GHz and above. The high-frequency band had a two-junction circulator (QuinStar QCI-G0400802) terminated at mK to reduce back-propagating thermal noise from the HEMT. No suitable circulator was found for the low-frequency band. Instead, extra lumped element low-pass filters with 3.8 GHz cut-off frequencies were added. Finally, a 23 dB gain room temperature amplifier is used to increase the signal to VNA readout noise ratio and reduce the data taking average time.

KID nonlinear driving power estimation. The critical field is reached when the stored energy in the resonator is comparable to the condensate energy^{29,40}

$$\frac{P_{\text{feed}} Q_r}{2\pi f_r} \sim 2N_0 \Delta_0^2 V_L \quad (6)$$

where Q_r and f_r are the total quality factor and resonance frequency, respectively, N_0 is the single-spin density of electron states at the Fermi energy, $N_0 = 3.6 \times 10^{10} \mu\text{m}^{-3} \text{eV}^{-1}$ for Hf⁴¹, Δ_0 is the superconducting gap at zero temperature, and V_L is the inductor volume. The resulting power value is roughly -50 dBm. On the other hand, heating the quasiparticles to 40 mK results in significant change in f_r and Q_r according to the top panels in Fig. 2. Dissipation through quasiparticle-phonon coupling is significantly suppressed at low temperatures as^{30,42}

$$P_{\text{el-ph}} = V_L \Sigma (T_{\text{el}}^5 - T_{\text{ph}}^5) \quad (7)$$

where T_{el} and T_{ph} are the electron (quasiparticle) temperature and phonon temperature, respectively, and $\Sigma = 10^8 \sim 10^9 \text{Wm}^{-3} \text{K}^{-5}$ is the electron-phonon coupling constant.⁴³ The resulting power is -110 dBm to -100 dBm, matches well with the measurement.

Fitting function for S_{21} to extract Q_i and f_r We use the following Eq. 8

$$S_{21}(f) = |a| e^{i\theta_a} e^{-i2\pi\tau f} \left(1 - \frac{e^{i\phi} Q_r / Q_c}{\cos\phi (1 + 2iQ_r(1 - f/f_r))} \right) \quad (8)$$

where $|a|$ and θ_a are the overall gain and phase delay of the transmission line, including all the attenuation and amplification. Here, τ is the propagation time in the transmission line, which will introduce a phase shift proportional to the frequency f . The formula in the brackets is the simple resonant response when $\phi = 0$. The additional phase ϕ accounts for the skew of the resonance, or equivalently, a rotation around $(0, 0.5)$ on the I-Q complex plane due to imperfections in the transmission line. Finally, Q_c is the coupling quality factor and $Q_r = (1/Q_c + 1/Q_i)^{-1}$ is the total quality factor. Formulas of the same format but slightly different notations were also suggested by previous works⁴⁴. Here, the $\cos\phi$ term on the denominator removes the ϕ dependence in the off-resonance transmission amplitude $|a|$ and makes the fitting more robust.

Generalization of the Mattis-Bardeen model. The temperature dependence of Q_i and f_r follows the Mattis-Bardeen (M-B) theory on the complex conductivity of superconducting films³⁵. Specifically, we find that for Hf, a gap-broadening factor Γ can be introduced to better fit the data^{2,36,37}. For clarity, we reproduce the equations we adopted below, which can also be found in³⁶. The conductivities are

$$\frac{\sigma_1}{\sigma_n} = \frac{1}{\hbar\omega} \int_{-\infty}^{\infty} [f(E) - f(E + \hbar\omega)] \quad (9)$$

$$[\Re(n(E))\Re(n(E + \hbar\omega)) + \Re(p(E))\Re(p(E + \hbar\omega))] dE$$

$$\frac{\sigma_2}{\sigma_n} = \frac{1}{\hbar\omega} \int_{-\infty}^{\infty} [1 - 2f(E + \hbar\omega)] \quad (10)$$

$$[\Im(n(E))\Re(n(E + \hbar\omega)) + \Im(p(E))\Re(p(E + \hbar\omega))] dE$$

where $f(E, T) = 1/(1 + e^{E/k_B T})$ is the Fermi distribution, \Re means taking the real part, \Im means taking the imaginary part, and

$$n(E) \equiv \text{sgn}(E) \frac{E + i\Gamma}{\sqrt{(E + i\Gamma)^2 - \Delta^2}} \quad (11)$$

$$p(E) \equiv \text{sgn}(E) \frac{\Delta}{\sqrt{(E + i\Gamma)^2 - \Delta^2}} \quad (12)$$

$\text{sgn}(E)$ is $-1, 0, 1$ for $E < 0, E = 0, E > 0$, respectively, and the square roots are taken with real part ≥ 0 . The superconducting gap at finite temperature, Δ , is calculated by solving

$$\frac{1}{N_0 V} = \int_0^{\hbar\omega_c} \frac{\tanh(\sqrt{E^2 + \Delta^2}/2k_B T)}{\sqrt{E^2 + \Delta^2}} dE \quad (13)$$

numerically, where ω_c is a cutoff frequency that is sufficiently large to avoid divergence of the integral. Here, we choose $\hbar\omega_c = 100\Delta_0$ and $\Delta_0 = 1.74k_B T_c$ is the zero temperature superconducting gap. The total number of states $N_0 V$ is estimated by setting $\Delta = \Delta_0$ and $T \rightarrow 0$.

Finally, the quasiparticle density, n_{qp} , can be written as

$$n_{\text{qp}} = 4N_0 \int_0^{\infty} f(E)\Re(n(E)) dE \quad (14)$$

ACKNOWLEDGMENTS

We thank the Nanofabrication facility at the Molecular Foundry in Lawrence Berkeley National Laboratory for sample annealing, the SEEQC, inc. for microfabrication, and the STAR Cryoelectronics, inc. for hafnium film deposition. This work is supported by the U.S. DOE, Office of High Energy Physics and Quantum Information Science Enabled Discovery (QUANTISED) for High Energy Physics, Office of Science, Office of Basic Energy Sciences, under Contract DE-AC02-05CH11231.

- ¹P. K. Day, H. G. LeDuc, B. A. Mazin, A. Vayonakis, and J. Zmuidzinas, “A broadband superconducting detector suitable for use in large arrays,” *Nature* **425**, 817–821 (2003).
- ²N. Zobrist, G. Coiffard, B. Bumble, N. Swimmer, S. Steiger, M. Daal, G. Collura, A. B. Walter, C. Bockstiegel, N. Fruitwala, *et al.*, “Design and performance of hafnium optical and near-ir kinetic inductance detectors,” *Applied Physics Letters* **115** (2019).
- ³K. Dibert, P. Barry, Z. Pan, A. Anderson, B. Benson, C. Chang, K. Karkare, J. Li, T. Natoli, M. Rouble, *et al.*, “Development of mkids for measurement of the cosmic microwave background with the south pole telescope,” *Journal of Low Temperature Physics* **209**, 363–371 (2022).
- ⁴D. Moore, S. Golwala, B. Bumble, B. Cornell, P. Day, H. LeDuc, and J. Zmuidzinas, “Position and energy-resolved particle detection using phonon-mediated microwave kinetic inductance detectors,” *Applied Physics Letters* **100** (2012).
- ⁵D. J. Temples, O. Wen, K. Ramanathan, T. Aralis, Y.-Y. Chang, S. Golwala, L. Hsu, C. Bathurst, D. Baxter, D. Bowering, *et al.*, “Performance of a phonon-mediated kinetic inductance detector at the nexu cryogenic facility,” *Physical Review Applied* **22**, 044045 (2024).
- ⁶A. Cruciani, L. Bandiera, M. Calvo, N. Casali, I. Colantoni, G. Del Castello, M. del Gallo Roccagiovine, D. Delicato, M. Giammei, V. Guidi, *et al.*, “Bullkid: Monolithic array of particle absorbers sensed by kinetic inductance detectors,” *Applied Physics Letters* **121** (2022).
- ⁷W. Guo, X. Liu, Y. Wang, Q. Wei, L. Wei, J. Hubmayr, J. Fowler, J. Ullom, L. Vale, M. Vissers, *et al.*, “Counting near infrared photons with microwave kinetic inductance detectors,” *Applied Physics Letters* **110** (2017).
- ⁸P. K. Day, N. F. Cothard, C. Albert, L. Foote, E. Kane, B. H. Eom, R. Basu Thakur, R. M. Janssen, A. Beyer, P. M. Echternach, *et al.*, “A 25-micrometer single-photon-sensitive kinetic inductance detector,” *Physical Review X* **14**, 041005 (2024).
- ⁹O. Noroozian, J. A. Mates, D. A. Bennett, J. A. Brevik, J. W. Fowler, J. Gao, G. C. Hilton, R. D. Horansky, K. D. Irwin, Z. Kang, *et al.*, “High-resolution gamma-ray spectroscopy with a microwave-multiplexed transition-edge sensor array,” *Applied Physics Letters* **103** (2013).
- ¹⁰S. Sypkens, L. Minutolo, S. Patel, E. Knehr, A. B. Walter, H. G. Leduc, L. Narváez, R. Chamberlin, T. Jamison-Hooks, M. D. Shaw, P. K. Day, and B. Korzh, “Frequency-domain multiplexing of snspds with tunable superconducting resonators,” *Applied Physics Letters* **124**, 262602 (2024), https://pubs.aip.org/aip/apl/article-pdf/doi/10.1063/5.0220090/20011699/262602_1_5.0220090.pdf.
- ¹¹Y. Kahn and T. Lin, “Searches for light dark matter using condensed matter systems,” *Reports on Progress in Physics* **85**, 066901 (2022).
- ¹²S. A. Hertel, A. Biekert, J. Lin, V. Velan, and D. McKinsey, “Direct detection of sub-gev dark matter using a superfluid he 4 target,” *Physical Review D* **100**, 092007 (2019).
- ¹³C. Fink, S. Watkins, T. Aramaki, P. Brink, S. Ganjam, B. Hines, M. Huber, N. Kurinsky, R. Mahapatra, N. Mirabolfathi, *et al.*, “Characterizing tes power noise for future single optical-phonon and infrared-photon detectors,” *AIP Advances* **10** (2020).
- ¹⁴S. Knapen, J. Kozaczuk, and T. Lin, “Python package for dark matter scattering in dielectric targets,” *Physical Review D* **105**, 015014 (2022).
- ¹⁵R. Anthony-Petersen, C. L. Chang, Y.-Y. Chang, L. Chaplinsky, C. W. Fink, M. Garcia-Sciveres, W. Guo, S. A. Hertel, X. Li, J. Lin, *et al.*, “Low energy backgrounds and excess noise in a two-channel low-threshold calorimeter,” *arXiv preprint arXiv:2410.16510* (2024).
- ¹⁶G. Angloher, S. Banik, G. Benato, A. Bento, A. Bertolini, R. Breier, C. Bucci, J. Burkhart, L. Canonica, A. D’Addabbo, *et al.*, “First observation of single photons in a cress detector and new dark matter exclusion limits,” *Physical Review D* **110**, 083038 (2024).
- ¹⁷M. Albakry, I. Alkhatib, D. Alonso-González, D. Amaral, J. Anczarski, T. Aralis, T. Aramaki, I. Arnquist, I. Atee Langroudy, E. Azadbakht, *et al.*, “Light dark matter constraints from supercdms hvev detectors operated underground with an anticoincidence event selection,” *Physical Review D* **111**, 012006 (2025).
- ¹⁸R. Anthony-Petersen, A. Biekert, C. Chang, Y. Chang, L. Chaplinsky, A. Dushkin, C. Fink, M. Garcia-Sciveres, W. Guo, S. Hertel, *et al.*, “Demonstration of the herald superfluid helium detector concept,” *Physical Review D* **110**, 072006 (2024).
- ¹⁹B. A. Mazin, “Superconducting materials for microwave kinetic inductance detectors,” in *Handbook of Superconductivity* (CRC Press, 2022) pp. 756–765.
- ²⁰N. Booth, “Quasiparticle trapping and the quasiparticle multiplier,” *Applied physics letters* **50**, 293–295 (1987).
- ²¹K. D. Irwin, S. W. Nam, B. Cabrera, B. Chugg, and B. A. Young, “A quasiparticle-trap-assisted transition-edge sensor for phonon-mediated particle detection,” *Review of Scientific Instruments* **66**, 5322–5326 (1995).
- ²²C. Fink, S. Watkins, T. Aramaki, P. Brink, J. Camilleri, X. Defay, S. Ganjam, Y. G. Kolomensky, R. Mahapatra, N. Mirabolfathi, *et al.*, “Performance of a large area photon detector for rare event search applications,” *Applied Physics Letters* **118** (2021).
- ²³B. A. Mazin, B. Bumble, P. K. Day, M. E. Eckart, S. Golwala, J. Zmuidzinas, and F. A. Harrison, “Position sensitive x-ray spectrophotometer using microwave kinetic inductance detectors,” *Applied physics letters* **89** (2006).
- ²⁴S. B. Kaplan, C. Chi, D. Langenberg, J.-J. Chang, S. Jafarey, and D. Scalapino, “Quasiparticle and phonon lifetimes in superconductors,” *Physical Review B* **14**, 4854 (1976).
- ²⁵G. Coiffard, M. Daal, N. Zobrist, N. Swimmer, S. Steiger, B. Bumble, and B. Mazin, “Characterization of sputtered hafnium thin films for high quality factor microwave kinetic inductance detectors,” *Superconductor Science and Technology* **33**, 07LT02 (2020).
- ²⁶K. Rotermond, X. Li, R. Carney, D. Yohannes, R. Cantor, J. Vivalda, A. Chambal-Jacobs, and A. Suzuki, “Development of hafnium-based transition edge sensor bolometers for cosmic microwave background polarimetry experiments,” *arXiv preprint arXiv:2410.06227* (2024).
- ²⁷S. Kraft, A. J. Peacock, M. Bavdaz, B. Castelletto, B. Collaudin, D. Perez, R. Venn, and T. E. Harper, “Use of hafnium-based superconducting tunnel junctions as high-resolution spectrometers for x-ray astronomy,” in *EUV, X-Ray, and Gamma-Ray Instrumentation for Astronomy IX*, Vol. 3445 (SPIE, 1998) pp. 226–235.
- ²⁸D. Goldie and S. Withington, “Non-equilibrium superconductivity in quantum-sensing superconducting resonators,” *Superconductor Science and Technology* **26**, 015004 (2012).
- ²⁹L. Swenson, P. Day, B. Eom, H. Leduc, N. Llombart, C. McKenney, O. Noroozian, and J. Zmuidzinas, “Operation of a titanium nitride superconducting microresonator detector in the nonlinear regime,” *Journal of Applied Physics* **113** (2013).
- ³⁰P. De Visser, S. Withington, and D. Goldie, “Readout-power heating and hysteretic switching between thermal quasiparticle states in kinetic inductance detectors,” *Journal of Applied Physics* **108** (2010).
- ³¹Sonnet Software, Inc., “Sonnet Simulation Software,” (2018).
- ³²A. Kerr, “Surface impedance of superconductors and normal conductors in em simulators,” *MMA Memo* **21**, 1–17 (1999).
- ³³J. Zmuidzinas, “Superconducting microresonators: Physics and applications,” *Annu. Rev. Condens. Matter Phys.* **3**, 169–214 (2012).
- ³⁴J. Gao, J. Zmuidzinas, A. Vayonakis, P. Day, B. Mazin, and H. Leduc, “Equivalence of the effects on the complex conductivity of superconductor due to temperature change and external pair breaking,” *Journal of Low Temperature Physics* **151**, 557–563 (2008).
- ³⁵D. C. Mattis and J. Bardeen, “Theory of the anomalous skin effect in normal and superconducting metals,” *Physical Review* **111**, 412 (1958).
- ³⁶M. Žemlička, P. Neillinger, M. Trgala, M. Reháč, D. Manca, M. Grajcar, P. Szabó, P. Samuely, S. Gaži, U. Hübner, *et al.*, “Finite quasiparticle lifetime in disordered superconductors,” *Physical Review B* **92**, 224506 (2015).
- ³⁷S. B. Nam, “Theory of electromagnetic properties of superconducting and normal systems. i,” *Physical Review* **156**, 470 (1967).
- ³⁸M. Skvortsov and M. Feigel’man, “Subgap states in disordered supercon-

- ductors,” *Journal of Experimental and Theoretical Physics* **117**, 487–498 (2013).
- ³⁹R. Barends, J. Baselmans, S. Yates, J. Gao, J. Hovenier, and T. Klapwijk, “Quasiparticle relaxation in optically excited high-q superconducting resonators,” *Physical review letters* **100**, 257002 (2008).
- ⁴⁰M. Tinkham, *Introduction to superconductivity*, Vol. 1 (Courier Corporation, 2004).
- ⁴¹O. Jepsen, O. K. Andersen, and A. R. Mackintosh, “Electronic structure of hcp transition metals,” *Physical Review B* **12**, 3084 (1975).
- ⁴²F. Wellstood, C. Urbina, and J. Clarke, “Hot-electron effects in metals,” *Physical Review B* **49**, 5942 (1994).
- ⁴³Estimated with the value of aluminum³⁰, assuming it is on the same order of magnitude in pure metals.
- ⁴⁴S. Probst, F. Song, P. A. Bushev, A. V. Ustinov, and M. Weides, “Efficient and robust analysis of complex scattering data under noise in microwave resonators,” *Review of Scientific Instruments* **86** (2015).